Batteries & Supercaps

Articles
doi.org/10.1002/batt.202100048

Chemistry Europe
European Chemical
Societies Publishing

Liquid-Crystal Mediated Assembly of Iodinated Graphene Oxide for Ultra-Dense Supercapacitors as Safe Power Source for Internet of Things Data Transmission

Meysam Sharifzadeh Mirshekarloo,*[a] M. C. Dilusha Cooray,[a] Petar Jovanović,[a]
Christopher D. Easton,[b] Fan Wu,[c] Tanesh D. Gamot,[a] Md. Joynul Abedin,[a]
Mehmet Rasit Yuce,[c] Mahdokht Shaibani,[a] and Mainak Majumder*[a, d]

Dense iodinated reduced graphene oxide (rGO) with outstanding electrical and electrochemical properties is produced through a green method comprising liquid crystal-mediated assembly of polyiodides and GO, and subsequent UV irradiation. The dense rGO electrode (1.46 g/cm^3) exhibited a very high volumetric capacitance of 226 F/cm^3, a factor of three larger than commercial activated carbon, and amongst the highest reported for graphene. The scalability is demonstrated by the fabrication of supercapacitor pouch cells that realized a volumetric energy density of 0.94 Wh/l, comparable to market products with similar footprint, while advantageously using a safe and green aqueous electrolyte. Our pouch cell powered battery-less Internet of Things (IoT) sensor nodes and demonstrated sensing and transmission of over 40 temperature and relative humidity data packets. Our work establishes the critical advantages graphene-based materials have over activated carbons in terms of ease of fabrication, tailorability, and enhanced volumetric energy density to advance the state-of-art in supercapacitor device research.

1. Introduction

Supercapacitors are energy storage devices that store and release electrical charge through physical adsorption and desorption of ions. Despite their smaller energy density compared to batteries, their unlimited lifetime, higher power density and safer packaging promise better power source for emerging applications such as Internet of Things (IoT) and wireless sensor network (WSN). WSN refers to a group of spatially dispersed and dedicated sensors for monitoring and recording the physical conditions of the environment and organizing the collected data at a central location.[1] The realization of the true potential of IoT and WSN, has been slowed down due to the limited lifetime of the sensor node, mainly constrained by the limited lifetime of the power source, usually batteries.[2] Moreover, the hermetic packaging requirement for batteries, adds size and cost implications, otherwise, the safety of the system will be seriously challenged.

While demonstrating almost unlimited cycle life and greatly improved safety over batteries, the volumetric energy density of the thin supercapacitors designed for IoT applications lags behind, ranging from around 0.3 to 0.8 Wh/l for state-of-the-art CapXX Thinline HW109T series.[3] Activated carbon (AC) electrodes of commercial supercapacitors are highly porous to facilitate the rapid diffusion and transport of ions. The highly porous nature of the electrodes, however, results in a very low packing density (0.3–0.7 g/cm^3), and consequently poor volumetric energy density. An immediate solution could be the replacement of the 3D activated carbon with a 2D graphene electrode. However, the promising gravimetric performance metrics of the graphene electrodes do not often translate to high volumetric figures given the poor packing densities of the electrodes.[4]

Furthermore, the presence of the toxic tetraethylammonium tetrafluoroborate salt in the organic electrolyte[5] still imparts limitations in the use of supercapacitors, either AC-based or graphene-based, in wearables, where ultimate safety is essential. This narrows down the choices of the power source to aqueous supercapacitors. This choice, unfortunately, limits the maximum operation voltage to 1 V, which then significantly reduces the gravimetric/volumetric capacitance of current electrodes and consequently, the energy density of the device.

While, improving the capacitance of AC materials has reached the limits, graphene-based electrodes are yet to

[a] Dr. M. S. Mirshekarloo, Dr. M. C. D. Cooray, P. Jovanović, Dr. T. D. Gamot,
    Dr. M. J. Abedin, Dr. M. Shaibani, Prof. Dr. M. Majumder
    Nanoscale Science and Engineering Laboratory (NSEL),
    Department of Mechanical and Aerospace Engineering
    Monash University
    Clayton, VIC 3168, Australia
    E-mail: meysam.sharifzadehmirshekarloo@monash.edu
            mainak.majumder@monash.edu
[b] Dr. C. D. Easton
    Manufacturing
    Commonwealth Scientific and Industrial Research Organisation (CSIRO)
    Ian Wark Laboratories, Clayton, Victoria 3168, Australia
[c] Dr. F. Wu, Prof. Dr. M. R. Yuce
    Department of Electrical and Computer System Engineering
    Monash University
    Clayton, Victoria 3168, Australia
[d] Prof. Dr. M. Majumder
    ARC Research Hub for Graphene Enabled Industry Transformation
    Monash University
    Clayton, VIC 3800, Australia

⬛ Supporting information for this article is available on the WWW under
    https://doi.org/10.1002/batt.202100048

Batteries & Supercaps

Articles
doi.org/10.1002/batt.202100048

Chemistry Europe
European Chemical
Societies Publishing

demonstrate their full performance potential. A common practice to maintain the large gravimetric capacitance of graphene at practical level loadings and discharge rates (milliseconds) is to induce a 3D porous network.[6] However, the best of the reported graphene-based electrode materials in terms of gravimetric capacitance, such as reduced multilayer graphene oxide (RMGO),[7] laser-scribed rGO (LSG),[8] and 3D graphene hydrogel prepared via hydrothermal reduction[9] demonstrate a low to medium packing density (0.05–0.75 g/cm³). The low packing density substantially jeopardizes the specific volumetric capacitance of the electrode.[4] Further, the highly porous electrode adversely affects the gravimetric energy density of the supercapacitor at the package level due to the increased amount of electrolyte required to fill the large empty spaces in the electrode. For example, a chemically converted graphene electrode in which the graphene sheets remained largely separated, gave rise to a large gravimetric capacitance (> 200 F/g), due to the facilitated ion transport, however, the very low packing density (≈ 0.07 g/cm³), resulted in a mediocre volumetric capacity (≈ 18 F/cm³)[10] – considerably smaller than that of commercial activated carbon (≈ 50–100 F/cm³).[11] Further, the empty spaces in the electrode will result in excess uptake of the electrolyte without adding capacitance (increasing the weight of the device unduly).[12]

The production of porous yet densely packed graphene electrodes with good pore interconnectivity and ion accessibility through scalable methods has proved to be a formidable challenge. Yang et al.,[4] successfully introduced liquid-mediated highly compact graphene-based electrodes with packing density of up to ≈ 1.5 g/cm³, nearly double that of best graphene and AC materials. At a mass loading of 2 mg/cm² and packing density of 1.5 g/cm³, the volumetric capacitance of the liquid electrolyte-mediated chemically converted graphene (EM-CCG) was measured to be (≈ 180 F/cm³) at the current density of 0.1 A/g, a marked improvement compared to that of the other carbon-based electrodes.[4] However, the effective preparation of solution-processable rGO from graphene oxide typically involves a hydrazine/HI reduction and a solvent exchange step. The use of hydrazine/HI in large-scale implementation is not plausible due to its high toxicity and potential explosion hazards.[13] Furthermore, the complexity of the solvent exchange process hinders the scalability of the electrode fabrication.

In short, the complicated manufacturing process and the low volumetric performance are the main reasons why the breakthrough innovations around graphene electrodes struggle to find their way from laboratory discovery to the market. Alternative sustainable and scalable strategies to make high-quality rGO electrodes is critical for the fabrication of safe supercapacitors that deliver the required levels of volumetric energy density for WSN applications.

Herein we show that relying on the discotic nematic liquid crystalline phase of GO and the use of Potassium iodide (KI) salt as a unique source of stable and non-toxic iodide, we can readily form large-sized and uniform partially reduced GO (PrGO) electrodes by means of the industrially adaptable blade coating technique. The presence of iodide imparts substantial

deoxygenation of GO *in-situ*. To further promote the reduction of the PrGO electrode, we treat the film with ultraviolet (UV) light with a wavelength of 254 nm (UVC), which in line with the first step, eliminates the need for the use of harmful materials and elevated temperatures distinguishing our method from others. Herein, we show that the presence of iodine in the PrGO film holds the key to the quality properties that are achieved upon UV treatment. Iodine acts as a spacer and prevents the undesired restacking of graphene upon reduction. In addition, the atomically and molecularly adsorbed iodine withdraws electrons from graphene surfaces, and by doing so promotes high electrical conductivity and induces improved graphitization.[14]

Our alternative green approach for reducing large size GO films enables the production of ultra-packed rGO electrodes with similarly good ion accessibility even at higher packing densities (up to 1.46 g/cm³). At areal mass loadings of 1.5–2 mg/cm² and using Li₂SO₄ aqueous electrolyte, our UV-converted iodinated graphene electrodes delivered a remarkable volumetric capacitance of 226 F/cm³ at a current density of 0.1 A/g. This is almost three times higher than that of Maxsorb (80 F/cm³),[15] and amongst the highest reported values for graphene-based supercapacitor electrodes (50–120 F/cm³[16] and 100–234 F/cm³).[17]

2. Results and Discussion

2.1. PrGO Suspension and Partial Reduction Mechanism

Owing to its liquid crystalline nature, GO is one of the most versatile and processable forms of carbon. When reduced, however, the suspension loses its nematic properties, jeopardizing its processability, and tends to settle quickly when stored. Figure 1 has summarized our approach to addressing this problem by synthesizing stable PrGO suspension, which is then used to fabricate dense supercapacitor electrodes with high volumetric capacitance.

The PrGO suspension was synthesized by mixing different ratios of GO liquid crystal (GOLC) and KI (PrGO $x:y$) at room temperature in a vacuum mixer (Figure 1a). To bring the innovative processing into context, we noted that many of the literature approaches use highly toxic HI[18] or the unstable/oxidizing NaI/HCl[19] for iodine-mediated reduction of GO, which effectively hinders their translation to industry. KI, on the other hand, is the stable, cheap, and non-toxic salt of iodine with numerous applications in the medicine and food industry.

The immediate partial reduction of GO in the presence of KI was confirmed through a set of complementary experiments – this is a beneficiary phenomenon that sets favorable conditions for the subsequent processing steps. First, GO:KI mixtures with different ratios were coated and dried on Ni foil (Figure 1b). The dried films were then extensively washed with reverse osmosis (RO) water to remove the excess KI, and used for further characterization to explore the structural, chemical, and electrical variations advantageously induced by KI. The effective removal of excess KI from washing was examined using XPS
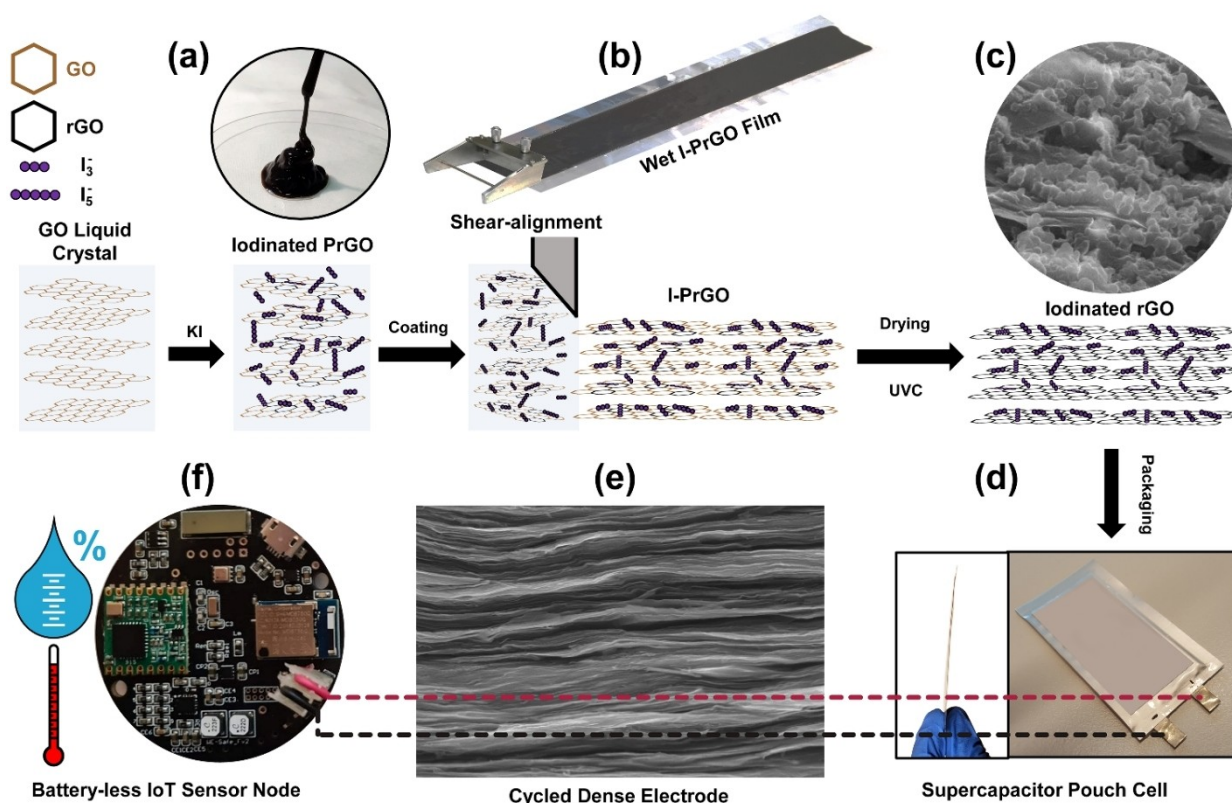
Figure 1. Schematic overview of the synthesis of iodinated PrGO suspension and the process of fabrication of iodinated rGO-based supercapacitors to power a battery-less IoT sensor node. GO is first dispersed in DI water to form GOLC (a) and then mixed with KI in an appropriate ratio to yield I-PrGO (b). The I-PrGO is then coated and dried on Ni foil through a shear alignment process using a doctor blade (c) and subsequently reduced to iodinated rGO film by illumination to UVC light. The I-rGO electrodes are then calendered and packaged into a compact supercapacitor pouch cell (d), thanks to the dense structure of the rGO electrode (e). The supercapacitor is then interfaced directly with a battery-less sensor node, which measures and transmits environmental data (f).

analysis; washing was continued until the K 2p doublet from KI was eliminated (Figure S2).

Reduction of GO during the mixing process was apparent from the X-ray diffraction analysis of the substantially washed GO:KI films (Figure 2a). While the XRD pattern of GO exhibited a single peak at $2\theta \sim 12.2°$, attributed to the $GO_{(001)}$ planes with an interlayer spacing of $d_{001,GO} \sim 7.3$ Å, after mixing with KI in 1:2 ratio, the peak slightly shifted to a larger 2θ angle $\sim 12.9°$ and a new broad peak appeared at $2\theta \sim 21.4°$. The shift of $GO_{(001)}$ peak indicates a reduction in interlayer spacing of GO ($d_{001,GO} \sim 6.9$ Å) due to the removal of some of the functional groups and the appearance of the new peak is attributed to the development of $rGO_{(002)}$ planes with an interlayer spacing of $d_{002,rGO} \sim 4.2$ Å. This indicates the formation of a mixed GO and rGO suspension when GO is mixed with KI, hence the realization of PrGO.

While GO makes a highly stable suspension in water, its reduction tends to disrupt the stability and result in settling of the reduced GO phase. Hence, it is crucial to examine the stability of the PrGO suspensions. Quite interestingly, after storing for a few days, the 20 g/L PrGO suspensions did not settle. To understand this result, we conducted zeta potential measurements for GO and different PrGO suspensions (Figure 2e).

Zeta potential of the pure GO suspension was measured at $\sim$-44 mV. The GO:KI ratio was found to strongly affect zeta potential of the PrGO suspensions; by adding KI, it initially increased to $\sim$-31 mV for PrGO 4:1. The initial increase may be attributed to the formation of some rGO, which reduces the stability of the suspension. With further increase of KI, the zeta potential started to decrease and dropped to below that of pure GO, a sign of improved stability. With the addition of more KI and further removal of functional groups, the high electrostatic negative charges may be screened by the net positive charges due to the presence of K^+ ions.

On the other hand, the electrostatic repulsion from the adsorbed I^- ions could assist in effective dispersion of rGO in the aqueous phase resulting in the reduction of the zeta potential, which yields a stable PrGO suspension. Furthermore, similar to GO, PrGO 1:2 suspension was found to exhibit optical retardance in the polarized light microscopy analysis (Figure 2f,g and Figure S6) with the liquid crystal domains clearly visible. However, PrGO exhibited smaller domains compared to GO probably because presence of partially reduced sheets tends to disturb the long-range interactions between the GO sheets.[21]

X-ray photoelectron spectroscopy revealed a partially deoxygenated structure for the synthesized PrGO. The survey spectra of GO and PrGO are presented in Figure 3a. The atomic
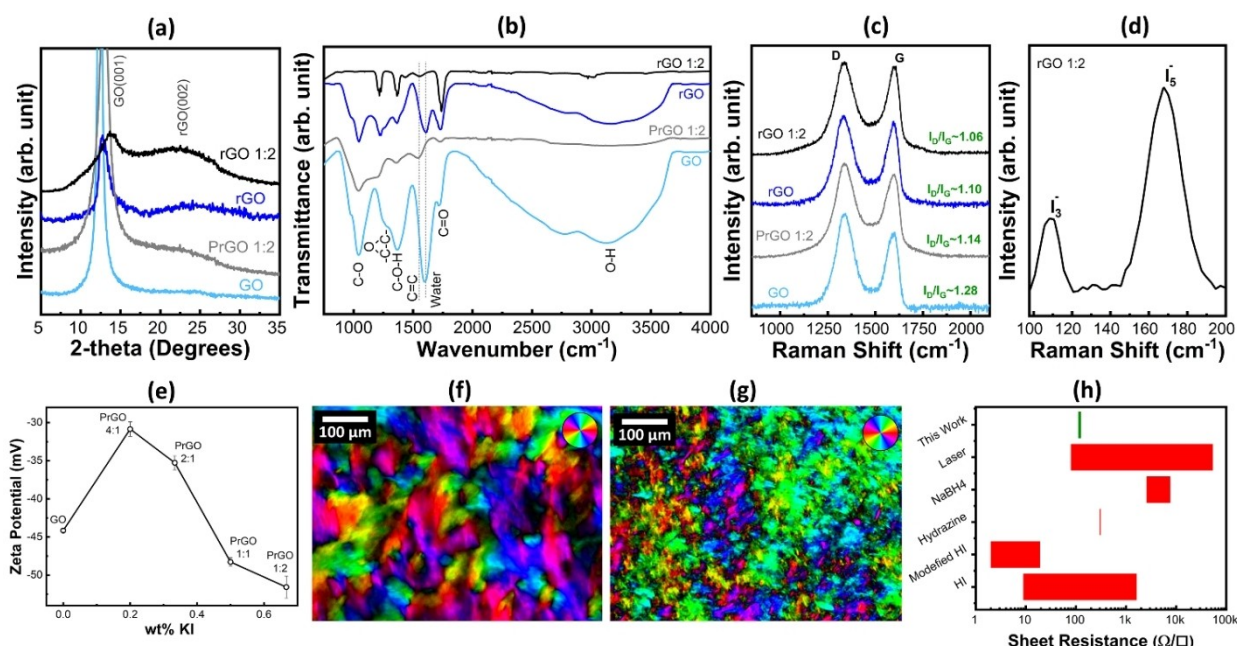
Figure 2. a) X-Ray diffractograms, b) FTIR, and c) Raman spectra of the GO and PrGO films and their UV reduced rGO counterparts; d) low-frequency Raman spectrum of rGO 1:2 film revealing the presence of polyiodides; all samples were washed with RO water before analysis to remove excess KI. e) Zeta potential of the GO and PrGO suspensions with various GO:KI ratios indicating improvement of stability of the suspension by increasing the KI content; pseudo-colored polarized light microscopy micrographs of f) GO, and g) PrGO 1:2 suspensions showing the liquid crystalline nature of GO and the disruption of the nematic domains with KI addition. h) Sheet resistance of the produced rGO films in comparison with the data reported in the literature.[18a,20]

concentrations of the detected elements calculated from the survey spectra are summarized in Table S1. Mixing with KI was found to result in immediate deoxygenation of GO and hence the C/O ratio increased from 2.46 (GO) to 2.94 (PrGO 1:2). The high-resolution C 1s spectra of GO and PrGO 1:2 (Figure 3b) revealed a reduction in the intensity of the peak assigned to C–O bonds of hydroxyl and epoxide moieties. This was in good agreement with FTIR analysis, which revealed a substantial reduction in the intensity of the peaks belonging to C–O–H, C–O–C and C–O functional groups compared to GO (Figure 2b). In addition, a significant decrease in the peak intensities of the OH groups, in hydroxyl and carbonyl moieties, and water molecules, integrated into the GO sheets,[22] was further evident from the FTIR analysis. Both XPS and FTIR results suggest that the C=O bonds in carboxyl and carbonyl groups, were persistent and remained intact during the mixing process.

The simple addition of KI to GO can lead to a number of simultaneous and complementary reactions upon mixing. These are: (i) Given the acidic nature of our starting GO suspension (pH < 3) and the presence of H$^+$, halogen ions such as iodine and bromine can catalyze an epoxide ring-opening reaction to yield hydroxyl moieties. The hydroxyls can consequently be reduced by an alcohol iodination reaction, hence the removal of epoxy (C–O–C) and hydroxyl (–OH) groups as suggested by the FTIR in Figure 2b.[18] (ii) In acidic conditions, the hydroxyl is protonated by an oxonium ion and the carbon of the C–O bond undergoes a nucleophilic attack by the iodide ion to give a C–I bond. A study found that a similar substitution reaction was possible by bromide, and the bromination of

graphene oxide resulted in the bromine substitution of hydroxyl groups.[23] Unlike C–Br bonds, dehydrohalogenation of C–I bonds is spontaneous, due to their lower dissociation energy of 213.4 kJ/mol compared to 284.5 kJ/mol,[24] and leads to a disproportionation reaction which yields graphene and iodine (I$_2$). (iii) It is known that molecular iodine (I$_2$) favorably catalyzes the dehydration of hydroxyls, to cleave the C–O bond.[25] While I$_2$ is not soluble in water, the presence of iodide ions I$^-$ greatly enhances I$_2$ solubility in aqueous solutions. In the presence of iodide ions I$^-$, I$_2$ may react further to form polyiodides such as I$_3^-$, and further to I$_5^-$ and I$_7^-$ in an acidic environment.[26]

The presence of polyiodides in the PrGO films, prior to washing, is evident in the low-frequency Raman and high resolution I 3d$_{5/2}$ XPS spectra. The low-frequency Raman spectra (Figure S3) of the unwashed PrGOs showed two strong bands at ~109 cm^{-1} and ~167 cm^{-1}. In addition, a weak band at ~130 cm^{-1} and a shoulder at ~140–145 cm^{-1} were also present. The two bands at 109 and 130 cm^{-1} signify the presence of triiodide (I$_3^-$), and the band at 167 cm^{-1} is the signature of the pentaiodide (I$_5^-$) species.[27] The presence of the weak shoulder at 140–145 cm^{-1} indicates the coexistence of symmetric and asymmetric I$_3^-$ ions. Since the Raman spectrum did not have any band at 185 cm^{-1}, presence of free molecular iodine (I$_2$) can be excluded.

The presence of high order polyiodides was further evident in the XPS analysis of the PrGO films. The I 3d$_{5/2}$ spectra of the unwashed PrGO 4:1, 2:1, and 1:2 films (Figure S4a-c) revealed the presence of 3 peaks, components I1 (618.6–618.7 eV), I2 (619.5–620.4 eV), and I3 (621.6–622.2 eV), attributed to I$_3^-$, and
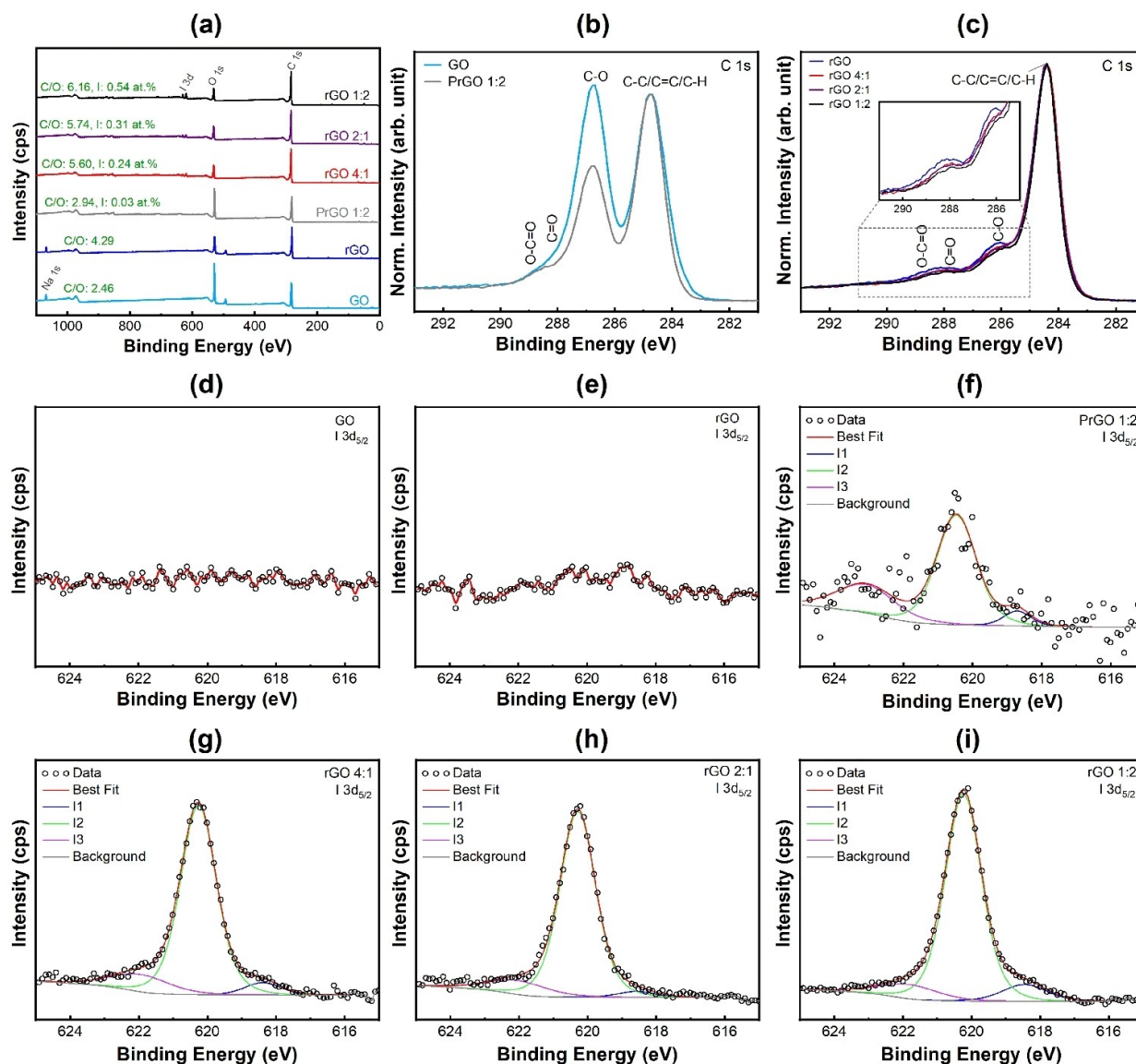
Figure 3. a) XPS survey spectra of GO and PrGO films before and after UVC reduction; b) comparison of the high-resolution C 1s spectra of GO and PrGO 1:2 films demonstrating removal of C—O bonds due to KI mixing; c) high-resolution C 1s spectra of UVC reduced GO and PrGO films with different GO:KI ratios; d-i) high-resolution I $3d_{5/2}$ spectra and the corresponding curve fitting for GO, rGO, PrGO 1:2, rGO 4:1, rGO 2:1, and rGO 1:2 showing the presence of polyiodides (mainly I_3^-, component I1, and I_5^-, component I2) in the PrGO and UVC reduced PrGO films. All of the samples were substantially washed with RO water to remove the excess KI.

I_5^- ions and a small shake-up satellite peak, respectively. This agrees with the Raman studies. The greater variation in the binding energy of the I_5^- ions may be due to the complex chemical environment in these samples, such as the coexistence of pentaiodide species with different molecular geometry or I—I bonds with variable strength due to the neighboring structure of the pentaiodide ions. The concentration of the I_5^- ions was found to increase with the increased KI content, possibly due to the presence of more I^- ions which are subsequently adsorbed by I_2 molecules and I_3^- ions to form I_5^-. The presence of free I^- ions in the PrGO films was excluded as observed by Raman (Figure S3).

Therefore, we propose that a follow-on and complimentary reaction between I_2 and the hydroxyl groups on GO also contribute to reduction. The removal of hydroxyl and epoxide moieties is evident in the FTIR analysis in Figure 2b, and the XPS C 1s spectra in Figure 3b with a reduction in the intensity of the C—O—C and C—O peaks. Both mechanisms suggest the reduction of GO, as observed in our experiments.

In addition to reactions leading to reduction of GO, the iodide S_N2 substitution of hydroxyls and subsequent disproportionation reaction leads to corresponding olefins[28] and is therefore instrumental in the restoration of the sp² network. This is supported by the observed decrease in I_D/I_G ratio (1.28 for GO to 1.14 for PrGO 1:2) as found from the Raman analysis (Figure 2c). The D band in Raman spectrum arises from the breathing modes of sp² atoms in carbon and requires a defect for activation. The G band, on the other hand, corresponds to

Batteries & Supercaps

Articles
doi.org/10.1002/batt.202100048

**Chemistry
Europe**
European Chemical
Societies Publishing

the bond stretching of all pairs of sp^2 atoms in carbon rings and chains and is a measure of graphitization of the GO structure. Development of the $rGO_{(002)}$ peak in XRD pattern of PrGO (Figure 2a) and a new band centered at ~1552 cm^{-1} in the FTIR spectrum (Figure 2b), attributed to the in-plane vibrations of sp^2 carbon,[29] provide further evidence to the restoration of sp^2 network.

Restoration of sp^2 structure is rarely achieved in the thermal and chemical reduction; most of these methods result in a substantial increase in defects, especially when hydrazine is used as the reducing agent; an effect that has only been observed through HI-reduction.[20c,30] Compared to the impractical HI reduction, our KI-based process enables a facile route to sp^2 structure reconstruction. In addition, we found trace concentrations of residual polyiodides in the substantially washed PrGO 1:2 films. XPS analysis revealed the presence of 0.03 at% of iodine in the form of I_3^- and I_5^- ions suggesting Iodination of PrGO (Figure 3f). Due to the synergistic effects of the sp^2 structure restoration and iodination of PrGO, the substantially washed PrGO 1:2 film exhibited an order of magnitude smaller sheet resistance (2.0 MΩ/□) compared to GO (11.3 MΩ/□) (Table 1).

2.2. KI-Assisted UV Reduction and Graphitization of GO

In our previous paper, we discussed the mechanisms through which UVC irradiation leads to the effective reduction of GO.[31] In brief, when GO is exposed to UVC radiation, removal of oxygenated functional groups (mainly O−H and C−O functionalities), restoration of the sp^2 C=C bonds, and formation and growth of graphitic nanodomains happen concurrently, resulting in a graphitic rGO with a reduced sheet resistance (1.8 MΩ/□). In the presence of KI, the final UVC induced rGO product (rGO $x:y$) was found to exhibit substantially improved structural and electrical properties due to the synergistic UVC-induced reduction and the aforementioned GO and KI reactions.

XPS analysis revealed larger C/O ratios for rGO $x:y$ films, in the range of 5.60–6.16, and suppressed peaks belonging to the C−O functional groups, compared to pure rGO with C/O ratio of 4.29 (Table 1 and Figure 3a,c), suggesting overall better deoxygenation (up to ~45%) when KI was present. Comparing the FTIR spectra of rGOs with and without KI present (during reduction), (Figure 2b) revealed a significantly greater reduction and elimination of functional groups. It is worth noting the

nearly complete removal of hydroxyl, water, and C−O groups and significant suppression of the C−O−H, C−O−C peaks during UVC reduction in the presence of KI. Without KI, a considerable number of functional groups were left attached to the rGO structure.

In addition to improved deoxygenation, UVC reduction in the presence of KI was found to enhance the graphitization of rGO; critical to applications where higher electrical conductivity is required. This is supported by a further decrease of the characteristic I_D/I_G ratio in the Raman spectrometric analysis of the rGO 1:2 film (1.06) (Figure 2c). In addition, the XRD pattern of the rGO 1:2 film exhibited a significantly suppressed $GO_{(001)}$ peak, which shifted to larger 2θ angle (13.7° corresponding to a $d_{001,GO}$ spacing of 6.4 Å), and a remarkably enhanced $rGO_{(002)}$ peak at $2\theta \sim 21.9°$ ($d_{002,rGO} \sim 4.1$ Å) (Figure 2a). Finally, the FTIR analysis showed that rGO 1:2 film exhibited a more distinguished C=C band (Figure 2b). In contrast, as one can see in Figure 2a and c, UVC-reduced pure GO film (rGO) exhibited a larger I_D/I_G ratio ~1.10 (Raman), a stronger $GO_{(001)}$ peak and a smaller $rGO_{(002)}$ peak (XRD). These observations clearly suggest the facilitated graphitization of rGO during UVC reduction and in the presence of KI.

2.3. Iodination of rGO

Iodination of rGO, induced by interactions between KI and GO, was revealed from the XPS analysis. The atomic concentration of iodine was 0.24 at.%, 0.31 at.%, and 0.54 at.% in the extensively washed rGO 4:1, 2:1, and 1:2 films, respectively (Table I and Figure 3a). Peak fitting of the high-resolution I $3d_{5/2}$ spectra of the substantially washed rGO $x:y$ films (Figure 3g-i) revealed the presence of triiodide and pentaiodide ions and a shake-up satellite. The presence of the polyiodides in the substantially washed rGO 1:2 was also confirmed by the presence of the bands at 109 and 167 cm^{-1} in the low-frequency Raman analysis (Figure 2d). Hence, our method provides an efficient means to introduce dopants to rGO.

Doping of iodine is through surface adsorption rather than ion implantation. The covalent doping of iodine into the structure of graphene, even under UVC irradiation as a catalyst, is unlikely. Homolytic bond cleavage of I_2 by UV light and subsequent chemical doping of iodine by free radical halogenation is highly endothermic and energetically unfavorable because the energy released from the H−I bond is insufficient to compensate for the energy needed to break the C−H bond. We believe the UVC irradiation further catalyzes and shifts the equilibrium of the reaction towards higher-order polyiodide formation (I_5^-). This is supported by the XPS analysis of the rGO $x:y$ films (Figure 3g-h and Figure S4d-f). A previous investigation of KI photochemistry in an acidic environment at irradiation of 254 nm (same as this study) proposed that the iodide ion absorbs light and leads to an aqueous electron via a charge transfer to solvent, forming an iodine radical ($I^•$), which can react further to shift the equilibrium towards polyiodide formation.[32] Arguably, the water molecules adsorbed between the lamella of GO,[33] which is also confirmed with our FTIR

Table 1. Carbon to oxygen ration, polyiodide concentration, and sheet resistance of the substantially washed films.

	C/O	Polyiodide concentration [at %]	Sheet resistance [Ω/□]
GO	2.46	0.00	11.3×10^6
rGO	4.29	0.00	1.8×10^6
PrGO 1:2	2.94	0.03	2.0×10^6
rGO 4:1	5.60	0.24	906.5
rGO 2:1	5.74	0.31	453.2
rGO 1:2	6.16	0.54	113.3

Batteries & Supercaps

Articles
doi.org/10.1002/batt.202100048

**Chemistry
Europe**

European Chemical
Societies Publishing

analysis, are believed to provide the water necessary to promote this UVC-catalyzed reaction.

2.4. Superior Electrical Properties of the Iodinated rGO

The effect of iodine doping on sheet resistances of the substantially washed rGO $x{:}y$ films was rather significant. Despite the modest increase in the degree of deoxygenation compared to UV-reduced pure GO (rGO), with the C/O ratio increasing from 4.29 to a range of 5.60–6.16 at different ratios of GO:KI when placing PrGO under UVC irradiation (rGO $x{:}y$), we witnessed a dramatic reduction in the sheet resistance by several orders of magnitude (from 1.8 MΩ/$\square$ for rGO to 113 Ω/$\square$ rGO 1:2). These observations show the role of polyiodides in improving the electrical conductivity of PrGO and rGO and are consistent with the HI reduced GO reported in the literature.[18] Because iodine and polyiodides are weak acceptors, they can create charge-transfer compounds with polymers[34] and carbon materials,[35] increasing their electrical conductivity. Further, it is believed that the electron transfer from the host to the polyiodide chains creates many mobile hole carriers, dramatically increasing the electrical conductivity.[36]

The polyiodide induced hole doping in our rGO $x{:}y$ films is supported by the observed 7 cm^{-1} blue shift in the G-band of the Raman spectrum.[37] It is noteworthy that compared to rGO 1:2, the d-spacing of (002) planes in rGO film was significantly smaller (3.6 Å compared to 4.1 Å), close to that of graphite ~ 3.4 Å, suggesting some restacking. The critically important higher d-spacing of rGO 1:2 is a further evidence of the presence of polyiodides physically adsorbed between the graphitic layers. Therefore, we believe that the dramatic decrease in sheet resistance is driven by a UVC-catalyzed reaction that favors the formation of polyiodides, which are then adsorbed on the restored sp^2 lattice of rGO, which act as a p-type surface dopant.

Figure 2(h) compares the sheet resistance of our produced rGO films with those reported in literature.[18a,20] The sheet resistance of our rGO is substantially lower than the laser, NaBH$_4$, and hydrazine reduced rGO films and comparable to those prepared by HI reduction while promising a scalable, appreciably simpler, and sustainable manufacturing process. With the low sheet resistance and high d-spacing, our Iodinated rGO films promise an ideal electrode material for high-performance energy storage devices.

2.5. Electrochemical Performance of the Iodinated rGO Films as Supercapacitor Electrodes

We used the rGO 1:2 films to construct electrical double-layer capacitors (EDLC) in a conventional coin cell using 1 M aqueous solution of Li$_2$SO$_4$ as the electrolyte. The cyclic voltammograms of the cells had a rectangular shape at the scan rates 5–100 mV/s, signifying the typical double-layer capacitive behavior of the electrode and its excellent rating capability (Figure 4a). As shown in the inset of Figure 4d, the galvanostatic

charge/discharge curves of the developed rGO electrodes measured at various current densities (0.2–5 A/g) had symmetric and linear profiles with a constant slope over the whole potential range resembling a nearly perfect double-layer capacitive behavior. The gravimetric capacitance of these electrodes, determined from the charge-discharge measurements at a current density of 0.1 A/g, was 154.1 F/g, translating to the electrode energy density of 22.3 Wh/kg. The fabricated iodinated rGO electrodes exhibited good capacitance retention of 80% with the increase of current density to 5 A/g (Figure 4b), resulting in an electrode power density of 8815.9 W/kg at a discharge time of 5.7 s. Furthermore, a very small IR drop was observed in the charge-discharge curves yielding a DC equivalent series resistance (ESR) of 6.1 Ω.

Figure 4c shows the Nyquist plot of the coin cell; the curve consisted of a small high-frequency semicircle and a high slope straight line in the low-frequency region. The small high-frequency semicircle represents a very small charge transfer resistance, and the low-frequency high slope straight line represents the capacitive nature of the electrodes. By extrapolating the vertical portion of the plot to the real axis, a DC ESR of ~6.5 Ω is found for the rGO, which is in good agreement with the charge-discharge measurements.

The long-term charge-discharge cycling performance of the coin cell was performed at a current density of 0.5 A/g. After an initial drop of about 13.5% in the specific capacitance after about 1000 cycles, the cell had a relatively stable long-term cycling performance with a retention of about 79.7% after 10,000 cycles (Figure 4d). This decrease is believed to be mainly due to the reaction of the remaining functional groups of rGO with electrolyte species.

In addition to the coin cell, pouch cell supercapacitor devices were also fabricated using the rGO electrodes (Figures 1d and S1). The CV curves of the pouch cell, measured at different scan rates, were similar to that of the coin cell (Figure S8). Furthermore, the specific capacitance of the rGO electrode, packaged in pouch cell format, was similar to that in coin cell resembling the scalability of the process. The pouch cell had enough energy to run a toy fan for a few minutes or keep an LED on for approximately an hour (Figure 4e).

At the device level, the pouch cell demonstrated competitive performance compared to commercial products with a similar footprint. Compared to the commercial CapXX Thinline HW109T series (energy density 0.24–0.54 Wh/Kg, 0.30–0.8 Wh/l),[3] our pouch cell realized a higher volumetric energy density of 0.94 Wh/l, despite using an aqueous electrolyte. This was achieved due to the higher density of packed rGO (Figure 1e), which is estimated to be about 1.46 g/cm^3 (based on the thickness of the pouch cell and its components); this is about 2–3 times that of the commercial activated carbon electrodes (0.45–0.70 g/cm^3).

The high-density rGO electrode yields a remarkable volumetric capacitance of $\approx$226 F/cm^3 at a current density of 0.1 A/g, almost three times higher than that of Maxsorb (80 F/cm^3),[15] and amongst the highest reported values for graphene-based supercapacitor electrodes (50–120 F/cm^3[16] and 100–234 F/cm^3).[17]

Batteries & Supercaps

Articles
doi.org/10.1002/batt.202100048

Chemistry Europe
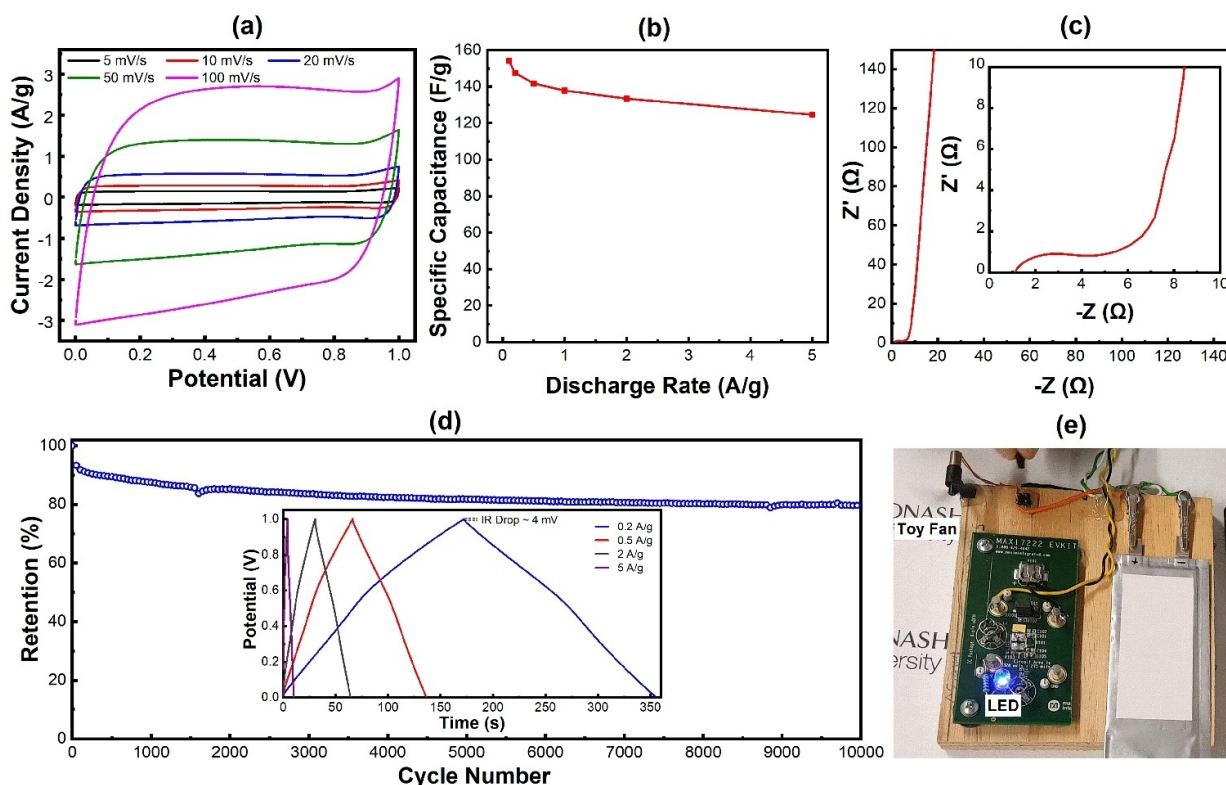European Chemical
Societies Publishing

Figure 4. a) Cyclic voltammograms of the supercapacitor coin cell made with the iodinated rGO electrodes; b) current density dependency of the specific capacitance of the electrodes; c) Nyquist diagram showing the electrical impedance behavior of the electrodes; d) long-term cycling data of the coin cell at the current density of 0.5 A/g over 10000 charge-discharge cycles, the inset shows the galvanostatic charge-discharge curves of the cell at different current densities; e) use of a 1 V pouch cell device made with the iodinated rGO electrodes to light up an LED and drive a toy fan.

2.6. Safe rGO Supercapacitors to Power Battery-Less IoT Sensor Node

To prove that the pouch cell can reliably supply power for continuous operation of IoT sensor nodes, we carried out an IoT test that utilizes the 1 V pouch cell as the energy storage unit for an environmental monitoring sensor node (Figure 1f). The pouch cell was pre-charged to 1 V and connected to the sensor node's nano-power boost converter. The boost converter regulates the energy from the supercapacitor and provides a constant 3.3 V for sensor node operation.

The IoT sensor node can detect temperature and relative humidity and then transmit the data via a long-range (LoRa) wireless module to a remote gateway. A block diagram and a photograph of the sensor node are presented in Figure 5a, b, respectively. It consists of a nano-power boost converter (MAX17222), a microcontroller (nRF52840 low-power system on chip), a LoRa wireless module (RFM95), and an environmental sensor (BME680). The sensor node is programmed to measure the surrounding environment every five seconds at different transmission powers. The full operation cycle for the sensor node consists of wake-up (50 ms), measure (100 ms), transmit (50 ms), and sleep (4800 ms). It consumes 5 mA in wake-up and measure mode and 3 μA in sleep mode. While in transmit mode, the sensor node is configured to transmit at the lowest transmission power of 2 dBm (30 mA) and the highest transmission power of 17 dBm (130 mA).

Figure 5c, d demonstrates the continuous voltage monitoring of the pouch cell under different transmission powers. Each voltage dip in the figure indicates a LoRa transmission. With 2 dBm transmission power, the pouch cell can support 41 LoRa wireless transmissions without any issue. With the highest 17 dBm transmission, the number of transmissions reduced to 28. Figure 5e, f demonstrates the collected environmental data with respect to the two different transmission powers. The data were successfully collected by the sensor node and transmitted to the gateway reliably. From the continuous voltage monitoring and the collected environmental data, it is seen that the aqueous rGO supercapacitor demonstrates promising capability as a safe energy storage unit for continuous energy supply for long-range IoT applications.

3. Conclusions

In summary, a facile and sustainable method for the synthesis of iodinated and dense rGO through the addition of KI salt and illumination under UV exposure is presented. The developed process eliminates the use of toxic chemicals such as hydrazine and HI while yielding an rGO with competitive electrical and electrochemical performance. The electrical conductivity of the synthesized iodinated rGO was as low as 113 Ω/□, comparable to that of HI reduced GO (ranging 10–1000 Ω/□). Owing to the high density (1.45 g/cm³) of the rGO, double layer super-
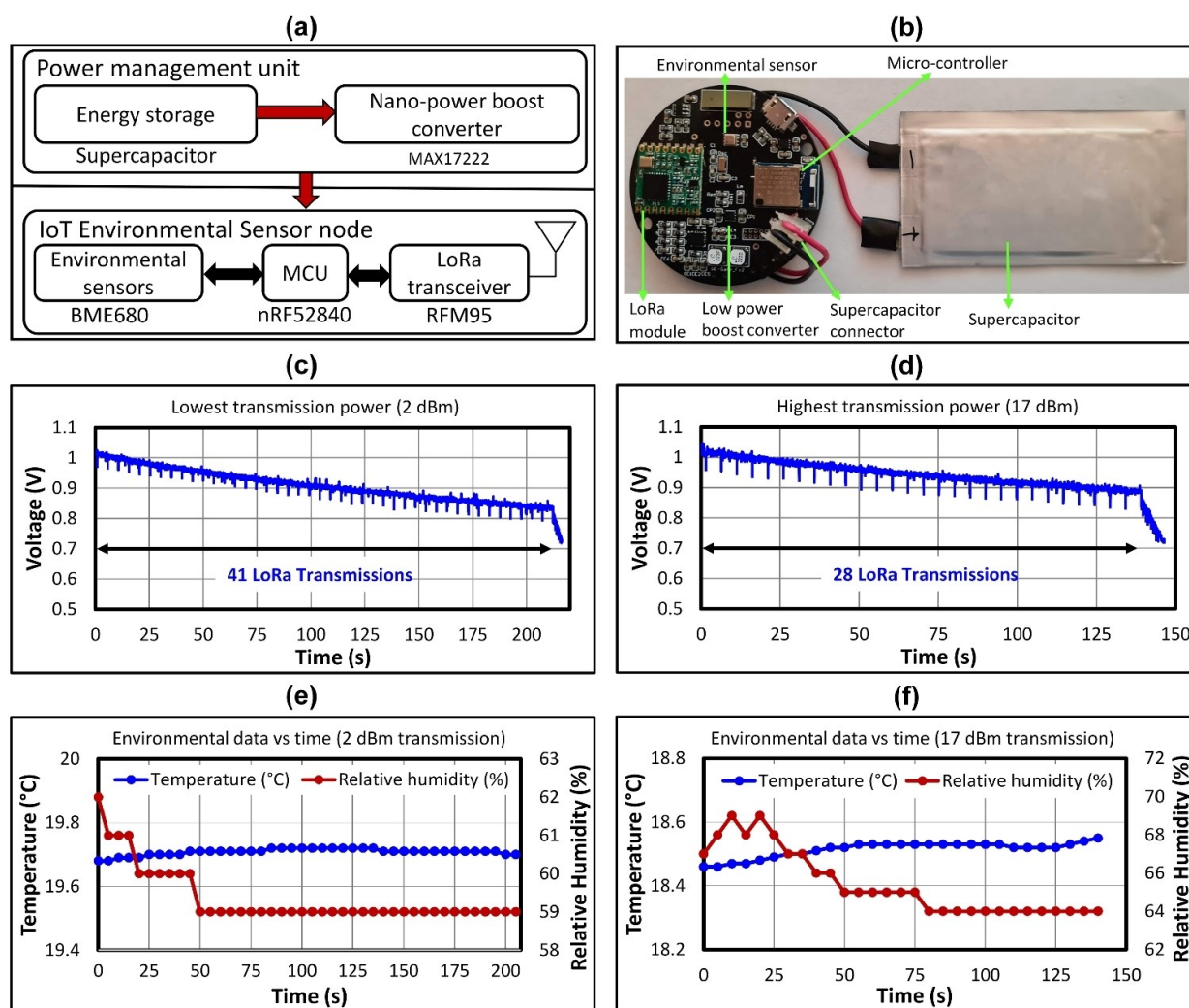
Figure 5. a) Block diagram of IoT sensor node; b) photograph of the IoT sensor node; c) continuous pouch cell voltage monitoring under 2 dBm transmission power; d) continuous pouch cell voltage monitoring under 17 dBm transmission power; e) 41 wireless environmental data transmissions at 2 dBm for 210 s; f) 28 wireless environmental data transmissions at 17 dBm for 140 s.

capacitor devices with exceptionally high volumetric capacitance and energy density were achieved. The packed rGO electrodes exhibited a volumetric capacitance of ≈ 226 F/cm³ at a current density of 0.1 A/g, almost 3 times higher than Maxsorb, and amongst the highest reported values for graphene-based supercapacitor electrodes. The pouch cell device had an outstanding volumetric energy density of 0.94 Wh/l, higher than the commercial CapXX Thinline HW109T series (0.30–0.80 Wh/l), successfully powered an IoT sensor node to sense and send environmental data for over 40 cycles in a single charge. This research opens new avenues for the development of safe, durable, and efficient power sources for various IoT and wearable applications.

Experimental Section

GO and PrGO suspensions

GO suspension, with concentration of ~20 g/L, was fabricated by liquid phase exfoliation of desalted graphite oxide (GtO) powders (supplied by The Sixth Element Inc.) in RO water, using a laboratory scale high speed high shear mixer (Silverson-L4RT) (Figure 1a). Subsequently, appropriate amounts of KI were mixed with the GO to achieve GO:KI ratios ranging from 4:1 to 1:2 in weight. The mixture was initially stirred at room temperature in a vacuum mixer and then re-exfoliated using the shear mixer to achieve a uniform partially reduced GO (PrGO) suspension (Figure 1b). Depending on the GO:KI ratio, the PrGO suspensions were designated as PrGO x:y where x and y are GO and KI weight fractions.

Zeta potentials of the GO and PrGO suspensions were measured at room temperature using a Brookhaven Nanobrook Omni Zeta Potential Analyzer. For each sample, average value from five measurements, with each measurement consisting of 20 phase cycles, was taken. For the measurement, a palladium electrode was slowly immersed in a polystyrene cuvette. With 1.0 cm path length

of polystyrene cuvette, Zeta potential, ζ, was determined using the Smoluchowski approximation [Eq. (1)]:

$$u_E = \frac{\vartheta_E}{E} = \frac{\zeta_\varepsilon}{\eta} \qquad (1)$$

where, u_E is the electrophoretic mobility, ϑ_E is the electrophoretic velocity, E is the electric field strength, ε is the permittivity and η is the viscosity of the medium.

Polarized light microscopy was carried out using an inverted Leica DM IRB Microscope fitted with Abrio polarizing imaging system from CRI, Inc. Images were taken at birefringence set-up mode comprising a linear polarizer, an analyzer and two variable electro-optical retarder plates instead of the traditional compensator. The polarized light transmitted through the specimen, loaded in a clean traditional microscopic glass slide, passed through an analyzer, and finally captured in a sensitive CCD camera. The captured signals were successively processed using a digital image processing system to generate the optical retardance and slow axis orientation images of the anisotropic material.

Fabrication of rGO films

GO and PrGO films of different GO:KI ratio were coated on Ni foil using a doctor blade (Figure 1c) followed by drying in a convection oven at 80 °C. The films were then reduced for 3 h under UV exposure using a UVC, 300 W, XPES globe enclosed in a mirrored protective box. The lamp had a fairly monochromatic spectrum with a wavelength of 254 nm. During the exposure, samples were placed at a distance of 5 cm away from the UV lamp and the chamber temperature was maintained at 80 °C by air ventilation. For structural investigations, the fresh or reduced films were extensively washed in RO water to remove the excess KI followed by compressed air rinse to remove the surface water and drying in convection oven at 80 °C. Finally, vacuum drying at 80 °C for 24 h was performed to fully dry the films. Similar to the suspensions, the rGO films were nominated as rGO x:y where x and y are GO and KI ratios.

For the subsequent structural and chemical characterization, the samples were washed extensively with RO water to remove the excess KI.

Morphology and crystal structure characterization

Scanning electron microscopy (SEM, FEI Nova NanoSEM 450 FEG) was used to investigate the morphology of the films. Secondary electron images were collected at an acceleration voltage of 5 kV and a working distance of 5 cm. X-ray diffraction (XRD) patterns were acquired in the 2θ range of 5–35° using a Bruker D2 phaser diffractometer with Cu–Kα radiation generated at 30 kV and 10 mA at a scan rate of 2°/min and a step size of 0.02°.

Determination of chemical structure

X-ray photoelectron spectroscopy (XPS) was conducted for in-depth investigation of chemical structure of the GO, PrGO and rGO films. XPS analysis was performed using an AXIS Nova spectrometer (Kratos Analytical Inc., Manchester, UK) details of which are provided in the supporting information. Fourier Transform Infrared spectroscopy (FTIR) was performed using an attenuated total reflectance Fourier Transform Infrared spectrometer (ATR-FTIR) (PerkinElmer, USA) in the wavenumber range of 750–4000 cm^{-1} at an average of 32 scans with a resolution of 2 cm^{-1}. Raman spectra

of the films were obtained using a Renishaw Confocal micro-Raman Spectrometer equipped with an Ar-ion (514 nm) green laser operating at 10% power. Extended scans (10 s) were performed between 100 and 3200 wavenumbers with a laser spot size of 1 μm. Once the background was removed, the intensity of the spectra was normalized by dividing the data by the maximum intensity. Peak fitting was carried out using the PeakFit software package and the fitted curves were used to determine the I_D/I_G ratios.

Fabrication and testing of EDLCs

To demonstrate application of the developed rGO films for energy storage applications, double-layer supercapacitor devices were constructed. Unwashed rGO films were used for this purpose. First rGO 1:2 electrodes were prepared on Ni foil following the procedure described above. The electrodes were then compacted using a two-roll calender equipment at ambient temperature and then packaged in a coin cell as well as pouch cell configuration. The pouch cell consisted a pair of folded electrodes (with dimensions of 6×6 cm^2) separated by a separator soaked in 1 M Li$_2$SO$_4$ electrolyte. Step by step fabrication process of the rGO supercapacitor pouch cell is shown in Figure S1. The electrochemical performance of the cells was measured at ambient condition using a BioLogic Potentiostat. Electrochemical impedance spectroscopy (EIS), cyclic voltammetry (CV) and galvanostatic charge-discharge measurements were performed following the procedure provided in the supporting information.

Battery-less IoT sensor node employing the I-rGO EDLCs

A sensor node is a device within a wireless sensor network that can measure its surrounding environment, process data, and communicate with other sensor nodes or a remote gateway via a wireless link. The sensor node consisted of an energy storage unit (i.e., the rGO-based supercapacitor) to supply energy for reliable operation of the sensor node, a power management unit to regulate and provide constant voltage for the rest of components, a microcontroller (MCU), a wireless module, and sensors.

Conflict of Interest

The authors declare no conflict of interest.

Batteries & Supercaps

Articles
doi.org/10.1002/batt.202100048

Chemistry Europe
European Chemical
Societies Publishing

[1] a) L. J. Liu, L. Ding, D. L. Zhong, J. Han, S. Wang, Q. H. Meng, C. G. Qiu, X. Y. Zhang, L. M. Peng, Z. Y. Zhang, *ACS Nano* **2019**, *13*, 2526–2535; b) J. S. Lee, J. Oh, J. Jun, J. Jang, *ACS Nano* **2015**, *9*, 7783–7790; c) W. W. Liu, C. X. Lu, X. L. Wang, R. Y. Tay, B. K. Tay, *ACS Nano* **2015**, *9*, 1528–1542.

[2] a) S. Roundy, D. Steingart, L. Frechette, P. Wright, J. Rabaey, in *Wireless Sensor Networks*, Springer Berlin Heidelberg, Berlin, Heidelberg, **2004**, pp. 1–17; b) Y. Q. Li, H. Y. Yu, B. Su, Y. H. Shang, *IEEE Sens. J.* **2008**, *8*, 678–681.

[3] in *CAP-XX Thinline Product Guide*, 3.1 ed. (Ed.: C.-X. A. P. Ltd), **2019**.

[4] X. Yang, C. Cheng, Y. Wang, L. Qiu, D. Li, *Science* **2013**, *341*, 534–537.

[5] a) R. Biczak, *J. Hazard. Mater.* **2016**, *304*, 173–185; b) F. Ghamouss, A. Brugere, J. Jacquemin, *J. Phys. Chem. C* **2014**, *118*, 14107–14123.

[6] X. Cao, Z. Yin, H. Zhang, *Energy Environ. Sci.* **2014**, *7*, 1850–1865.

[7] J. J. Yoo, K. Balakrishnan, J. Huang, V. Meunier, B. G. Sumpter, A. Srivastava, M. Conway, A. L. Mohana Reddy, J. Yu, R. Vajtai, *Nano Lett.* **2011**, *11*, 1423–1427.

[8] M. F. El-Kady, V. Strong, S. Dubin, R. B. Kaner, *Science* **2012**, *335*, 1326–1330.

[9] Y. Xu, Z. Lin, X. Huang, Y. Liu, Y. Huang, X. Duan, *ACS Nano* **2013**, *7*, 4042–4049.

[10] X. Yang, J. Zhu, L. Qiu, D. Li, *Adv. Mater.* **2011**, *23*, 2833–2838.

[11] M. Ghidiu, M. R. Lukatskaya, M.-Q. Zhao, Y. Gogotsi, M. W. Barsoum, *Nature* **2014**, *516*, 78.

[12] Y. Gogotsi, P. Simon, *Science* **2011**, *334*, 917–918.

[13] M. J. Fernández-Merino, L. Guardia, J. Paredes, S. Villar-Rodil, P. Solís-Fernández, A. Martínez-Alonso, J. Tascon, *J. Phys. Chem. C* **2010**, *114*, 6426–6432.

[14] D. Tristant, P. Puech, I. C. Gerber, *J. Phys. Chem. C* **2015**, *119*, 12071–12078.

[15] E. Raymundo-Piñero, F. Leroux, F. Béguin, *Adv. Mater.* **2006**, *18*, 1877–1882.

[16] L. Lu, *Vol. CN103253658 A* (Ed.: CNIPA), Changzhou Sixth Element Material Technology Co., Ltd., China, **2013**, p. 16.

[17] Y. X. Xu, C. Y. Chen, Z. P. Zhao, Z. Y. Lin, C. Lee, X. Xu, C. Wang, Y. Huang, M. I. Shakir, X. F. Duan, *Nano Lett.* **2015**, *15*, 4605–4610.

[18] a) S. F. Pei, J. P. Zhao, J. H. Du, W. C. Ren, H. M. Cheng, *Carbon* **2010**, *48*, 4466–4474; b) I. K. Moon, J. Lee, R. S. Ruoff, H. Lee, *Nat. Commun.* **2010**, *1*, 73.

[19] A. K. Nayak, A. K. Swain, in *Surface Engineering of Graphene*, Springer International Publishing, Cham, **2019**, pp. 259–271.

[20] a) Y. X. Xu, K. X. Sheng, C. Li, G. Q. Shi, *J. Mater. Chem.* **2011**, *21*, 7376–7380; b) R. Karthick, X. H. Hou, Q. Ru, S. S. Chandrasekaran, M. Ramesh, F. M. Chen, *RSC Adv.* **2019**, *9*, 33781–33788; c) S. Stankovich, D. A. Dikin, R. D. Piner, K. A. Kohlhaas, A. Kleinhammes, Y. Jia, Y. Wu, S. T. Nguyen, R. S. Ruoff, *Carbon* **2007**, *45*, 1558–1565; d) P. Cui, J. Lee, E. Hwang, H. Lee, *Chem. Commun.* **2011**, *47*, 12370–12372; e) D. A. Sokolov, C. M. Rouleau, D. B. Geohegan, T. M. Orlando, *Carbon* **2013**, *53*, 81–89; f) V. Strong, S. Dubin, M. F. El-Kady, A. Lech, Y. Wang, B. H. Weiller, R. B. Kaner, *ACS Nano* **2012**, *6*, 1395–1403; g) L. Huang, Y. Liu, L. C. Ji, Y. Q. Xie, T. Wang, W. Z. Shi, *Carbon* **2011**, *49*, 2431–2436; h) H. J. Shin, K. K. Kim, A. Benayad, S. M. Yoon, H. K. Park, I. S. Jung, M. H. Jin, H. K. Jeong, J. M. Kim, J. Y. Choi, Y. H. Lee, *Adv. Funct. Mater.* **2009**, *19*, 1987–1992.

[21] M. J. Abedin, T. D. Gamot, S. T. Martin, M. Ali, K. I. Hassan, M. S. Mirshekarloo, R. F. Tabor, M. J. Green, M. Majumder, *ACS Nano* **2019**, *13*, 8957–8969.

[22] a) A. M. Dimiev, S. Eigler, in *Graphene Oxide: Fundamentals and Applications*, 1 ed., John Wiley & Sons, Ltd., **2017**, pp. 85–120; b) A. M. Dimiev, L. B. Alemany, J. M. Tour, *ACS Nano* **2013**, *7*, 576–588.

[23] C. K. Chua, M. Pumera, *J. Mater. Chem.* **2012**, *22*, 23227–23231.

[24] S. C. Moldoveanu, in *Pyrolysis of Organic Molecules (Second Edition)* (Ed.: S. C. Moldoveanu), Elsevier, **2019**, pp. 1–33.

[25] G. L. Borosky, S. Stavber, K. K. Laali, *Top. Catal.* **2018**, *61*, 636–642.

[26] Y. Xie, M. R. McDonald, D. W. Margerum, *Inorg. Chem.* **1999**, *38*, 3938–3940.

[27] a) L. Mohanambe, S. Vasudevan, *Inorg. Chem.* **2004**, *43*, 6421–6425; b) S. B. Sharp, G. I. Gellene, *J. Phys. Chem. A* **1997**, *101*, 2192–2197.

[28] M. Konieczny, R. G. Harvey, *J. Org. Chem.* **1979**, *44*, 4813–4816.

[29] a) M. Acik, G. Lee, C. Mattevi, M. Chhowalla, K. Cho, Y. J. Chabal, *Nat. Mater.* **2010**, *9*, 840–845; b) A. Bagri, C. Mattevi, M. Acik, Y. J. Chabal, M. Chhowalla, V. B. Shenoy, *Nat. Chem.* **2010**, *2*, 581–587.

[30] A. Ganguly, S. Sharma, P. Papakonstantinou, J. Hamilton, *J. Phys. Chem. C* **2011**, *115*, 17009–17019.

[31] M. S. Mirshekarloo, M. Shaibani, M. C. D. Cooray, C. D. Easton, L. Bourgeois, S. Hernandez, P. Jovanovic, L. F. Dumee, P. C. Banerjee, M. Majumder, *ACS Sustainable Chem. Eng.* **2020**, *8*, 1031–1042.

[32] R. O. Rahn, *Photochem. Photobiol.* **1993**, *58*, 874–880.

[33] H. C. Bi, K. B. Yin, X. Xie, J. Ji, S. Wan, L. T. Sun, M. Terrones, M. S. Dresselhaus, *Sci. Rep.* **2013**, *3*, 2714–2717.

[34] X. R. Zeng, T. M. Ko, *J. Polym. Sci. Part B* **1997**, *35*, 1993–2001.

[35] L. Grigorian, K. A. Williams, S. Fang, G. U. Sumanasekera, A. L. Loper, E. C. Dickey, S. J. Pennycook, P. C. Eklund, *Phys. Rev. Lett.* **1998**, *80*, 5560–5563.

[36] a) R. A. Hoyt, E. M. Remillard, E. D. Cubuk, C. D. Vecitis, E. Kaxiras, *J. Phys. Chem. C* **2017**, *121*, 609–615; b) D. Tristant, P. Puech, I. C. Gerber, *Phys. Chem. Chem. Phys.* **2015**, *17*, 30045–30051.

[37] S. W. Chu, S. J. Baek, D. C. Kim, S. Seo, J. S. Kim, Y. W. Park, *Synth. Met.* **2012**, *162*, 1689–1693.